MNRAS 000, 1–11 (2019) Preprint 12 December 2021 Compiled using MNRAS LATEX style file v3.0

Modelling cosmic ray electron physics in cosmological smoothed particle hydrodynamics simulation

Dongchao Zheng [1] ⋆, Weitian Li [1], Zhenghao Zhu [1], Chenxi Shan[1], Jiajun Zhang[2]
Linfeng Xiao [1], Xiaoli Lian [1], Dan Hu[1],
[1]School of Physics and Astronomy, Shanghai Jiao Tong University, 800 Dongchuan Road, Shanghai 200240, China
[2]Center for Theoretical Physics of the Universe, Institute for Basic Science (IBS), Daejeon, 34126, Korea

arXiv:1912.00432v1 [astro-ph.HE] 1 Dec 2019

Accepted XXX. Received YYY; in original form ZZZ

ABSTRACT

Cosmic ray electron (CRE) acceleration and cooling are important physical processes in astrophysics. We develop an approximative framework to treat CRE physics in the parallel smoothed particle hydrodynamics code Gadget-3. In our methodology, the CRE spectrum of each fluid element is approximated by a single power-law distribution with spatially varying amplitude, upper cut-off, lower cut-off, and spectral index. We consider diffusive shock acceleration to be the source of injection, and oppositely the sinking processes is attributed to synchrotron radiation, inverse Compton scatters, and Coulomb scatters. The adiabatic gains and losses are also included. We show that our formalism produces the energy and pressure with an accuracy of $> 90\%$ for a free cooling CRE spectrum. Both slope and intensity of the radio emission computed from the CRE population given by our method in cosmological hydro-simulation coincide well with observations, and our results also show that relaxed clusters have lower fluxes. Finally, we investigate several impacts of the CRE processes on the cosmological hydro-simulation, we find that: (1) the pressure of the CRE spectrum is very small and can be ignored in hydro-simulation, (2) the impacts of the CRE processes on the gas phase-space state of hydro-simulation is up to 3%, (3) the CRE processes induce a 5% influence on the mass function in the mass range $10^{12} - 10^{13} h^{-1} M_{\odot}$, (4) The gas temperature of massive galaxy cluster is influenced by the CRE processes up to $\sim 10\%$.

Key words: galaxies:intergalactic medium - galaxies:clusters:general - acceleration of particles - radiation mechanisms: non-thermal - methods:numerical - cosmic rays

1 INTRODUCTION

Cosmological numerical simulation has become an indispensable tool in studying of the structure formation process of the universe (Springel et al. 2005b; Vogelsberger et al. 2014). There are currently three techniques employed in numerical simulations: (1) grid-based Eulerian schemes with optional adaptive mesh refinement (AMR; Bryan et al. 2014); (2) particle-based Lagrangian methods, namely the smoothed particle hydrodynamics (SPH; Monaghan 1992, 2005; Springel 2005, 2011a); (3) moving-mesh method (Springel 2010, 2011b) improving on the weakness of the SPH and AMR. In recent years, with the rapid growth of computer performance and the implementation of more sophisticated numerical algorithms, more complicated physical processes can be incorporated into numerical simulations. For example, the most popular TreeSPH code Gadget (**GA**laxies with **D**ark matter and **G**as int**E**rac**T**; Springel 2005), compared with its first version (Springel et al. 2001), includes many baryon physical processes, such as star formation (Springel & Hernquist 2003), cosmic ray proton (CRP; Enßlin et al. 2007; Jubelgas et al. 2008), cooling processes (Scholz & Walters 1991; Katz et al. 1996), shock wave (Pfrommer et al. 2006), thermal conduction (Jubelgas et al. 2004), radiative transfer (Petkova & Springel 2009), magnetohydrodynamics (MHD, Dolag & Stasyszyn 2009), black hole (Springel et al. 2005a; Sijacki et al. 2007), and so on.

One of the major radiation mechanisms in the radio band is the synchrotron radiation of cosmic ray electrons (CRE, Hoeft & Brüggen 2007). In order to trace the synchrotron radiation of CRE, we must know the spatial and energy distribution of CRE as well as the magnetic field. Since the MHD simulation can infer the magnetic field, how to obtain the properties of CRE in simulation is the key step to study the radio emission. The evolution of CRE spectrum is described by the Fokker-Planck equation (FP; Park & Petrosian 1995; Brunetti et al. 2004; Pinzke et al. 2017; Brunetti & Lazarian 2011), which can be solved numerically with the finite difference method (Chang & Cooper 1970; Park & Petrosian 1996; Donnert & Brunetti 2014). However, solving the FP equation is both

⋆ Contact e-mail: dczheng21@outlook.com

© 2019 The Authors

computation-intensive and memory-intensive. It is inappropriate to apply the finite difference method to large-scale cosmic simulations directly. Although Hoeft & Brüggen (2007) have proposed a novel method to compress the data of CRE spectrum to reduce memory usage, the computation-intensive problem still exists. Post-processing of simulation data is another choice, which solves the FP equation over many simulation snapshots (Pinzke et al. 2017). But this scheme takes into account neither the simulation information between snapshots nor the feedback of CRE physics. In this work, by analysing the CRE spectrum evolution governed by the FP equation, we find that a power-law distribution, characterised by spatially varying amplitude, upper and lower cut-offs, and spectral index, is a good approximation for the practical CRE dynamics. In such an approximate CRE framework, the intensive calculation of numerically solving the FP equation can be avoided, which is beneficial to investigating the CRE physical processes in cosmological hydro-simulation.

This paper is organized as follows: In Section 2, we describe our method to treat CRE physics in cosmological hydro-simulation. In Section 3, we discuss the radio emission calculated from the CRE population and the several impacts of the CRE processes on cosmological hydro-simulation. We conclude with a summary in Section 4.

2 COSMIC RAY ELECTRON PHYSICS AND MODELLING

2.1 Spectrum modelling of cosmic ray electron

The population of relativistic particles injected by various astrophysical processes (e.g., AGN activities, SNe.) can be approximated with a power-law distribution (Hoeft & Brüggen 2007; Enßlin et al. 2007; Jubelgas et al. 2008). Therefore, we assume that the CRE spectrum in each fluid element can be described by a single power-law with lower and upper cut-offs, i.e.

$$\begin{aligned} f(p) &= 4\pi p^2 f(\mathbf{p}) \\ &= \frac{dN}{dpdV} = Cp^{-\alpha}\,\Theta(p-p_{\rm min})\,\Theta(p_{\rm max}-p), \end{aligned} \tag{1}$$

where the dimensionless momentum $p = |\mathbf{p}|/m_e c$, $\mathbf{p}$ is electron momentum, m_e is the electron mass, c is the light speed, N is the number of electrons, V is the volume occupied by N electrons, C is the normalisation, α is the power-law slope, $p_{\rm min}$ and $p_{\rm max}$ are the upper and lower cut-offs, respectively, Θ(x) denotes the Heaviside step function. If $p_{\rm max}$ is infinity and $p_{\rm min} \equiv q$, the number density n, kinetic energy density ϵ, pressure P, and average kinetic energy $\overline{T} = \epsilon/n$ of CRE spectrum are (see appendix A for the detailed derivation):

$$n(C,\alpha,q) = \int_0^\infty dp f(p) = \frac{Cq^{1-\alpha}}{\alpha-1}, \tag{2a}$$

$$\begin{aligned} \epsilon(C,\alpha,q) &= \int_0^\infty f(p)T(p)dp = \frac{Cm_e c^2}{\alpha-1} \\ &\times\left[\frac{1}{2}B_{1/(1+q^2)}\left(\frac{\alpha-2}{2},\frac{3-\alpha}{2}\right)+q^{1-\alpha}\left(\sqrt{1+q^2}-1\right)\right], \end{aligned} \tag{2b}$$

$$\begin{aligned} P(C,\alpha,q) &= \frac{m_e c^2}{3}\int_0^\infty f(p)\beta p dp \\ &= \frac{Cm_e c^2}{6}B_{1/(1+q^2)}\left(\frac{\alpha-2}{2},\frac{3-\alpha}{2}\right), \end{aligned} \tag{2c}$$

$$\begin{aligned} \overline{T}(C,\alpha,q) &= \left[\frac{q^{\alpha-1}}{2}B_{1/(1+q^2)}\left(\frac{\alpha-2}{2},\frac{3-\alpha}{2}\right)\right. \\ &\left.+\sqrt{1+q^2}-1\right]m_e c^2, \end{aligned} \tag{2d}$$

where $T(p) = (\sqrt{1+p^2}-1)m_e c^2$ is the kinetic energy of a single electron with momentum p, $\beta = v/c = p/\sqrt{1+p^2}$ is the dimensionless velocity, and $B_x(a,b) = \int_0^x t^{a-1}(1-t)^{b-1}dt$ denotes the incomplete Beta function. Since there is no upper cut-off and $p_{\rm min} > 0$, these equations are valid for $\alpha > 2$. For finite $p_{\rm max}$, the values of n, ϵ, P and $\overline{T}$ can be derived from Eqs. 2.

2.2 Evolution of cosmic ray electron

The temporal evolution of CRE distribution $f(p,t)$ is governed by the isotropic, gyro-phase averaged FP equation (in the Lagrangian frame),

$$\begin{aligned} \frac{df(p,t)}{dt} &= \frac{\partial}{\partial p}\left\{f(p,t)\left[\left|\frac{dp}{dt}\right|_{\rm cool}-\frac{1}{p^2}\frac{\partial}{\partial p}(p^2 D_{\rm pp})\right]\right\} \\ &-(\nabla\cdot v)f(p,t)+\frac{\partial^2}{\partial p^2}\left[D_{\rm pp}f(p,t)\right]+Q\left[p,t;f(p,t)\right], \end{aligned} \tag{3}$$

where Q is the injection function, $d/dt = \partial/\partial t + v\cdot\nabla$ is the Lagrangian derivative, v is the gas velocity, the $\nabla\cdot v$ represents adiabatic gains and losses, $|dp/dt|_{\rm cool}$ represents Coulomb and radiative losses including synchrotron radiation and inverse Compton scattering (Hoeft & Brüggen 2007; Longair 2011; Pinzke et al. 2017), which are given by:

$$\left|\frac{dp}{dt}\right|_{\rm rad} = C_{\rm cool}p\sqrt{(1+p^2)}, \tag{4a}$$

$$\begin{aligned} \left|\frac{dp}{dt}\right|_{\rm coul} &= \frac{3c\sigma_T n_{\rm th,e}}{2\beta^2}\left\{\ln\left(\frac{m_e c^2\beta\sqrt{\gamma-1}}{\hbar\omega_{\rm plasma}}\right)\right. \\ &\left.-\ln(2)\left(\frac{\beta^2}{2}+\frac{1}{\gamma}\right)+\frac{1}{2}+\left(\frac{\gamma-1}{4\gamma}\right)^2\right\}, \end{aligned} \tag{4b}$$

with

$$C_{\rm cool} = \frac{4\sigma_T}{3m_e c}\left[(1+z)^4\frac{B_{\rm cmb,0}^2}{8\pi}+\frac{B^2}{8\pi}\right] \tag{4c}$$

$$\omega_{\rm plasma} = \sqrt{\frac{4\pi e^2 n_{\rm th,e}}{m_e}}, \tag{4d}$$

where σ_T is the Thomson cross-section, $B_{\rm cmb,0} \approx 3.24\,\mu$G is the equivalent magnetic field of the cosmic-microwave background at $z = 0$, and B is the magnetic field. $\gamma = \sqrt{1+p^2}$ is the Lorentz factor, $\omega_{\rm plasma}$ is the plasma frequency, $\hbar$ is the reduced Planck constant, $n_{\rm th,e}$ is the number density of thermal electron, and e is the electron charge. $D_{\rm pp}$ is the momentum space diffusion coefficient (Brunetti et al. 2004; Cassano & Brunetti 2005; Pinzke et al. 2017), which describes the turbulent acceleration. Compared to the diffusive shock acceleration (DSA) investigated in this work (see 2.3.1), the turbulent acceleration is relatively weak and inefficient, thus it is omitted in this work (i.e. $D_{\rm pp} = 0$).

2.3 Approximation method

In this subsection, we explain the approximation methods that are employed to determine the CRE spectrum parameters (i.e. $C, \alpha, p_{\rm min}, p_{\rm max}$ in Eqs. 2), avoiding numerically solving the FP equation (Eq. 3).

Since the CRE is implemented in Lagrangian code Gadget-3, it is convenient to normalise the physical quantities to mass instead of volume. Therefore we define

$$\widetilde{C} = \frac{C m_e}{\rho}, \tag{5a}$$

$$\tilde{n} = \frac{n m_e}{\rho}, \tag{5b}$$

$$\tilde{\epsilon} = \frac{\epsilon}{\rho}, \tag{5c}$$

$$\widetilde{P} = \frac{P}{\rho}, \tag{5d}$$

$$\overline{T} = \frac{\tilde{\epsilon}}{\tilde{n}} m_e, \tag{5e}$$

where ρ is the baryon density.

2.3.1 *Diffusive shock injection*

a. Detecting shock waves

Pfrommer et al. (2006) developed a formalism for the identification and accurate estimation of the strength of structure formation shocks on the fly in cosmological SPH-simulation. As they pointed out, the grid-based techniques offer superior capabilities in capturing shocks, while the dependence on the artificial viscosity is one drawback of SPH. Due to the broadening of shocks over the SPH smoothing scale, it can not be resolved as discontinuities, but the post-shock quantities can be calculated very accurately. We review their method of detecting shock in the following:

The shock surface separates two regions: the upstream region and downstream region, from which physical quantities (such as density ρ and pressure P) are labelled by 1 and 2, respectively. For a non-radiative polytropic gas, the conservation of mass, momentum, and energy flux allow us to derive the well-known Rankine-Hugoniot conditions (Landau & Lifshitz 1959; Pfrommer et al. 2006):

$$\frac{\rho_2}{\rho_1} = \frac{(\gamma_a + 1) M_1^2}{(\gamma_a - 1) M_1^2 + 2}, \tag{6a}$$

$$\frac{P_2}{P_1} = \frac{2\gamma_a M_1^2 - (\gamma_a - 1)}{\gamma_a + 1}, \tag{6b}$$

$$\frac{T_2}{T_1} = \frac{\left[2\gamma_a M_1^2 (\gamma_a - 1)\right] \left[(\gamma_a - 1) M_1^2 + 2\right]}{(\gamma + 1)^2 M_1^2}, \tag{6c}$$

where T is the temperature, $M_1 = v_1/c_{s1}$ is the Mach number in the upstream region with $c_{s1} = \sqrt{\gamma_a P_1/\rho_1}$ being the speed of sound, and γ_a being the adiabatic index.

Suppose that the shock is broadened to be the same order as the SPH smoothing length $f_h h$, where $f_h \sim 2$ is a calibrated factor (see Pfrommer et al. 2006) . The time for a particle to pass through the broadened shock front is estimated as $\Delta t \approx f_h h/v_1$. In Gadget, the entropic function is defined by $A \equiv P/\rho^{\gamma_a}$ (Springel 2005). The jump of the entropic function of particle between the shock surface is estimated as (Pfrommer et al. 2006)

$$\frac{A_2}{A_1} = \frac{A_1 + \Delta t dA_1/dt}{A_1} = 1 + \frac{f_h h}{M_1 c_1 A_1} \frac{dA_1}{dt}. \tag{7}$$

By substituting Eqs. 6a and 6b, into Eq. 7, we have

$$\begin{aligned} \frac{A_2}{A_1} &= \frac{P_2}{P_1} \left(\frac{\rho_1}{\rho_2}\right)^{\gamma_a} \\ &= \frac{2\gamma_a M_1^2 - (\gamma_a - 1)}{\gamma_a + 1} \left[\frac{(\gamma_a - 1) M_1^2 + 2}{(\gamma_a + 1) M_1^2}\right]^{\gamma_a}. \end{aligned} \tag{8}$$

By combining Eqs. 7 and 8, the final equation for estimating Mach number is

$$\left[f_A(M_1) - 1\right] M_1 = \frac{f_h h}{c_1 A_1} \frac{dA_1}{dt}, \tag{9a}$$

$$f_A M_1 = \frac{2\gamma_a M_1^2 - (\gamma_a - 1)}{\gamma_a + 1} \left[\frac{(\gamma_a - 1) M_1^2 + 2}{(\gamma_a + 1) M_1^2}\right]^{\gamma_a}. \tag{9b}$$

The right-hand side of Eq. 9a can be estimated individually for each particle, and the left-hand side depends only on M_1.

For a composite of CRP and thermal gas, the Mach number is derived with a similar procedure as the polytropic gas (see section 3.2 of Pfrommer et al. (2006) for more details). In cosmological simulation, the Mach number statistics generated by this method agree well with the results obtained with hydrodynamics mesh codes that use explicit Riemann solvers (Pfrommer et al. 2006). In addition, this scheme has a good convergence with different resolutions (Pfrommer et al. 2006; Vazza et al. 2011).

b. Injection

In DSA, particles are accelerated by multiple shock crossings (Fermi 1949). The energy spectrum of suprathermal electrons produced by DSA is well characterised by a power-law distribution. The spectral index $\alpha_{\rm inj}$ is determined by the compression ratio at shock front, i.e.

$$\alpha_{\rm inj} = \frac{r + 2}{r - 1}, \tag{10}$$

where $r = \rho_2/\rho_1$ denotes the shock compression ratio with ρ_2 and ρ_1 being the baryon density in downstream and upstream regimes of the shock, respectively.

We define the energy injection efficiency $\zeta_{\rm DSA}$ to be the energy density ratio of freshly injected CRE to the total dissipated energy in the downstream regime,

$$\zeta_{\rm DSA} = \frac{\epsilon_{\rm inj}}{\epsilon_{\rm dis}}, \tag{11a}$$

$$\epsilon_{\rm dis} = \epsilon_2 - \epsilon_1 r^{\gamma_a}, \tag{11b}$$

where ϵ_1 and ϵ_2 are the energy density in upstream and downstream region of the shock, respectively, $\epsilon_{\rm inj}$ is the injected energy density, and $\epsilon_{\rm dis}$ is the dissipated energy density which is the difference of the energy densities in the pre-shock and pos-shock region. In this work, we adopt $\zeta_{\rm DSA} = 0.005$ (Hoeft et al. 2008).

Even though we can account for CRE injection by shocks in SPH using the Mach finder developed by Pfrommer et al. (2006),

the shock broadening inherent in SPH is a problem, to receive the full dissipative energy, an SPH particle may require several timesteps before it has passed through a shock. Jubelgas et al. (2008) have faced the same problem in their DSA injection of CRP physics. As they pointed out, because the correct pre-shock and post-shock state fulfill the the conservation of energy in SPH code, the correct integration of $\epsilon_{\rm dis}$ through the shock profile will be accomplished by SPH code automatically. Therefore we can replace $\epsilon_{\rm dis}$ in Eq. 11a with the dissipated energy in the current timestep. Note that we remove the injection energy $\epsilon_{\rm inj}$ from the thermal pool.

The minimum momentum $p_{\rm inj}$ of DSA injection is an important parameter in determining the electron spectrum, because a significant fraction of energy, pressure, and number density are carried by the lower-energy part of the CRE spectrum. Following Hoeft & Brüggen (2007), we adopt $p_{\rm inj} = 10\,k_B T/m_e c^2$, suggesting that $p_{\rm inj}$ is tightly coupled with the temperature of the plasma.

Since the DSA process is very efficient, after DSA injection, we assume the lower cut-off, upper cut-off, and spectral index to be $p_{\rm inj}$, ∞ and $\alpha_{\rm inj}$, respectively. Thus the normalisation $\widetilde{C}$ is determined by numerically solving the equation:

$$\tilde{\epsilon}\left(\widetilde{C}, \alpha_{\rm inj}, p_{\rm inj}\right) = \tilde{\epsilon}_{\rm inj} + \tilde{\epsilon}_{\rm old}. \tag{12}$$

Note that we suppose that the injected spectrum and the new spectrum have no upper cut-off. Since we use the conservation of energy to derive the spectrum parameters in the injection process, the results of injection do not depend on the upper cut-off.

2.3.2 *Loss*

In this subsection, we analyse the cooling processes (Eqs. 4a, 4b) and describe the methods to determine the upper cut-off $p_{\rm max}$ and lower cut-off $p_{\rm min}$.

a. The upper cut-off $p_{\rm max}$

Lawson et al. (1987) has suggested that the upper energy limit of the DSA account for the steepening of the radio spectrum (Figure 7 of Lawson et al. (1987)). In this work, we assume that there is no upper cut-off for DSA injection (see Sec. 2.3.1) and attribute upper cut-off to the radiative losses (Eq. 4a), which dominate at high energy regime. Considering that the momentum of an electron decreases from p_0 at time t_0 to p_1 at time t_1, the conservation of energy gives:

$$\int_{p_0}^{p_1} \frac{dp}{p\sqrt{1+p^2}} = -\int_{t_0}^{t_1} C_{\rm cool}(t)dt, \tag{13}$$

where the time dependence of $C_{\rm cool}$ comes from the baryon magnetic field (Dolag & Stasyszyn 2009) and the the equivalent magnetic field of CMB. If the initial spectrum is a power law, then the final spectrum has a maximum momentum $p_{\rm max}$ given by:

$$\int_{\infty}^{p_{\rm max}} \frac{dp}{p\sqrt{1+p^2}} = -\int_{t_0}^{t_1} C_{\rm cool}(t)dt, \tag{14}$$

that is

$$\frac{1}{p_{\rm max}} = \sinh\left(\int_{t_0}^{t_1} C_{\rm cool}(t)dt\right), \tag{15}$$

where the the right hand side is computed by the accumulation of $C_{\rm cool}(t)$ in simulation. We use this maximum momentum $p_{\rm max}$ as our upper cut-off.

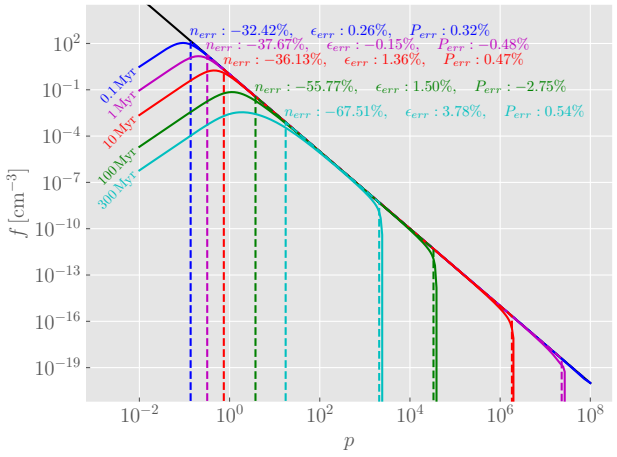


Figure 1. Evolution of CRE distribution. The initial CRE populations are discribed by $(C, \alpha, p_{\rm min}, p_{\rm max}) = (1, 2.5, 10^{-2}, 10^8)$. Spectra are shown for cooling ages of $\approx (0.1, 1, 10, 100, 300)$ Myr. The solid lines show the numerically exact solutions and the model solutions are displayed by dashed lines. $n_{\rm err}$, $\epsilon_{\rm err}$ and $P_{\rm err}$ are the relative difference of number density, energy density and pressure of CRE, respectively.

b. The lower cut-off $p_{\rm min}$

Since most energy and pressure are carried by low-momentum electrons and the energy and pressure are two ways for simulation to interact with the CRE processes, the lower cut-off $p_{\rm min}$ of our model must guarantee the accurate calculations of energy and pressure. On the other hand, the normalisation of spectrum is very sensitive to the lower cut-off for fixed total energy, so the lower cut-off will affect the radio emission. At low energy, the dominant losses will be the Coulomb loss. The calculation of Coulomb loss (Eq.4b) is complicated and some approximation should be adopted. To this end, we replace the momentum p in the curly braces of Eq.4b with its mean value for the given initial spectrum being $\langle p\rangle = p_{\rm min,0}(1-\alpha)/(2-\alpha)$, where $p_{\rm min,0}$ is the lower cut-off of the initial spectrum. Then, the dependence of momentum in the right hand side of Eq. 4b is only in β and Coulomb loss function, thus Eq.4b becomes

$$\left.\frac{dp}{dt}\right|_{\rm coul} \approx -\frac{C_{\rm coul}\left(\langle p\rangle, t\right)}{\beta^2}, \tag{16}$$

where $C_{\rm coul}$ is given by Eq. 4b and does not depend on the momentum p. The time dependence of $C_{\rm coul}$ comes from the number density of thermal electron $n_{\rm th,e}$. Considering that the momentum of an electron decreases from p_0 at time t_0 to p_1 at time t_1, the conservation of energy gives:

$$\int_{p_0}^{p_1} \beta^2 dp \approx -\int_{t_0}^{t_1} C_{\rm coul}\left(\langle p\rangle, t\right) dt. \tag{17}$$

If the electrons with momentum $p < p_{\rm cut}$ in an initial spectrum at time t_0 do not appear in the final spectrum at time t_1, then $p_{\rm cut}$ is given by

$$\int_{p_{\rm cut}}^{0} \beta^2 dp = p_{\rm cut} - \arctan(p_{\rm cut}) \approx -\int_{t_0}^{t_1} C_{\rm coul}\left(\langle p\rangle, t\right) dt, \tag{18}$$

where the integral on the left hand side is computed by the accumulation of $C_{\rm coul}(\langle p\rangle, t)$ in simulation.

Since the Coulomb losses vary slowly with p and result in a flat

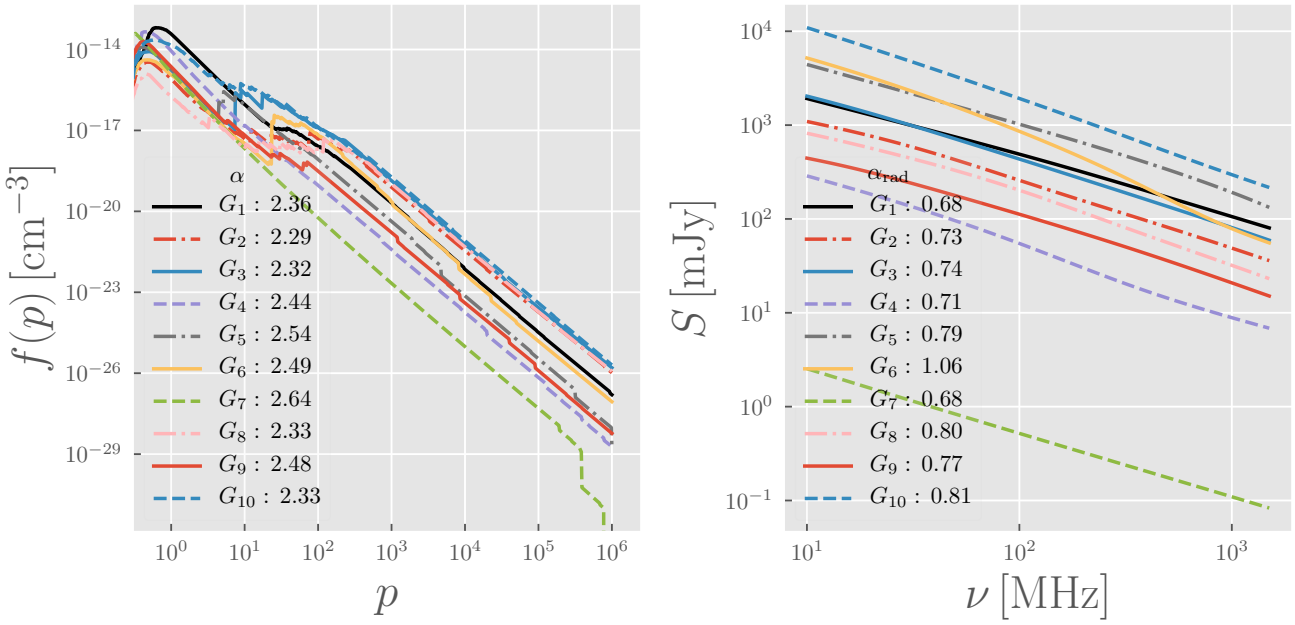


Figure 2. Integrated CRE distribution (left panel) and radio emission spectrum(right panel) of ten most massive clusters with $M > 10^{14} M_{\odot}$ at $z = 0.1$. α is the slope of electron spectrum in the momentum range $10^3 - 10^5$. α_{rad} is the spectral index of radio emission in the frequency range $0.3 - 1.4\,\mathrm{GHz}$.

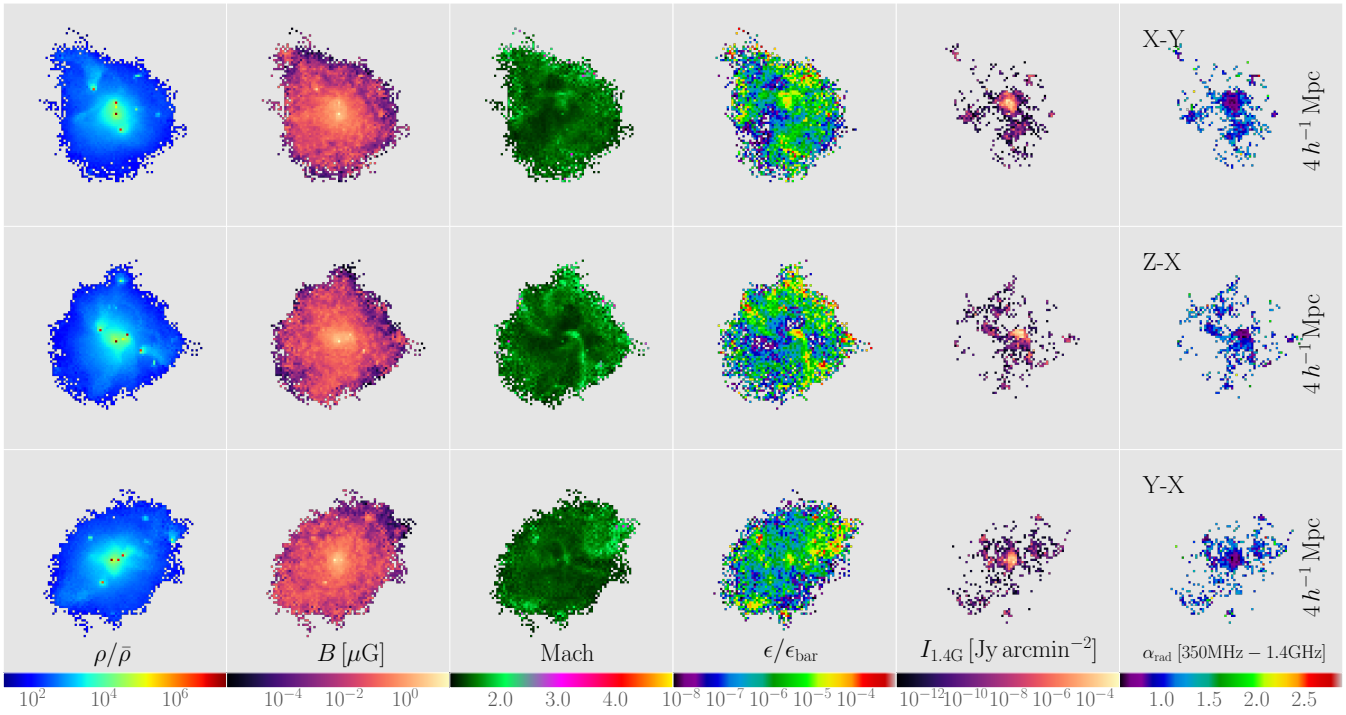


Figure 3. The three direction projection for the most massive cluster in SIM-CRE simulation taken from snapshot with $z = 0.1$. From left to right, baryon density, magnetic field, Mach number, CRE energy, radio emission of 1.4GHz, and the spectral index in 350MHz – 1.4GHz are shown. The projection cube has a comoving side length $5\,h^{-1}\mathrm{Mpc}$. ϵ_{bar} is the baryon energy.

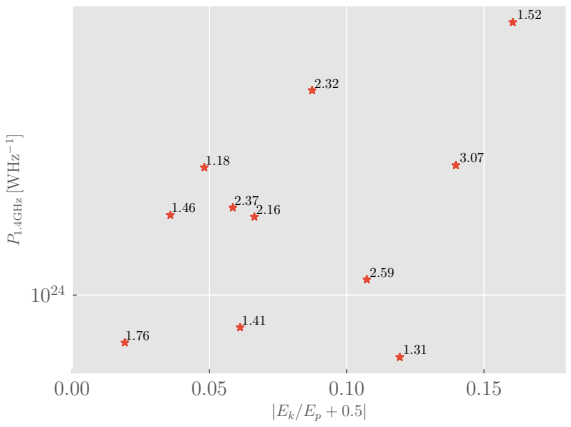


Figure 4. Ralation between radio power $P_{1.4\mathrm{GHz}}$ and the virialization state for some massive clusters with $P_{1.4\,\mathrm{GHz}} > 5 \times 10^{23}\mathrm{WHz}^{-1}$ and mass $M > 10^{14}h^{-1}M_{\odot}$, where E_k and E_p are the kinetic energy and potential energy.

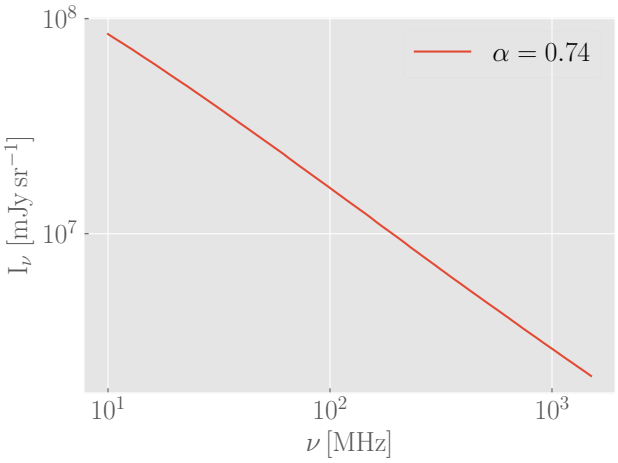


Figure 5. The radio background emission obtained from our SIM-CRE simulation.

spectrum (see Fig.1) at the low energy, using the p_{cut} as the lower cut-off will lead to an underestimate of the energy loss. Therefore we should consider the energy loss of electrons with momentum $p \geq p_{\mathrm{cut}}$. From Eq. 16 we can obtain the energy loss rate for a single electron:

$$\left.\frac{dT(p)}{dt}\right|_{\mathrm{coul}} = m_e c^2 \beta \left.\frac{dp}{dt}\right|_{\mathrm{coul}} \approx -m_e c^2 C_{\mathrm{coul}}(\langle p\rangle, t)\frac{1}{\beta}. \tag{19}$$

The energy losses of a single electron from time t_0 to t_1 is given by

$$\Delta T(p) = \int_{T_0}^{T_1} dT(p)dp \approx -\frac{1}{\beta}\int_{t_0}^{t_1} m_e c^2 C_{\mathrm{coul}}(\langle p\rangle, t)dt, \tag{20}$$

where T_0 and T_1 are the energy of the single electron at time t_0 and t_1, respectively. In order to obtain the total Coulomb loss of the CRE spectrum, we have to integrate above equation over the population

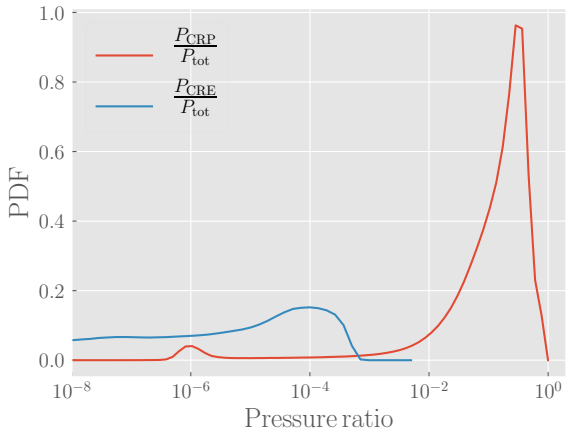


Figure 6. Probability Density Function (PDF) of the CRE pressure and CRP pressure of particles taken from the snapshot with reshift $z = 0$.

$f(p)$, i.e.

$$\begin{aligned}\Delta\tilde{\epsilon} = \frac{\Delta\epsilon}{\rho} &\approx -\frac{1}{\rho}\int_{p_{\mathrm{cut}}}^{\infty}\frac{f(p)}{\beta}dp\int_{t_0}^{t} m_e c^2 C_{\mathrm{coul}}(\langle p\rangle, t)dt \\ &= -\frac{\widetilde{C}}{\alpha}\left[\frac{1}{2}B_{\frac{1}{1+q_{\mathrm{cut}}}}\left(\frac{\alpha-1}{2}, \frac{2-\alpha}{2}\right) + q^{-\alpha}\sqrt{1+q^2}\right] \\ &\times \int_{t_0}^{t} C_{\mathrm{coul}}(\langle p\rangle, t)dt.\end{aligned} \tag{21}$$

Consequently, the lower cut-off of our model is determined by numerically solving the following equation:

$$\tilde{\epsilon}\left(\widetilde{C}, \alpha, p_{\mathrm{min}}\right) = \tilde{\epsilon}\left(\widetilde{C}, \alpha, p_{\mathrm{cut}}\right) + \Delta\tilde{\epsilon}\left(\widetilde{C}, \alpha, p_{\mathrm{cut}}\right). \tag{22}$$

Opposite to the radiative loss, this cooling energy will be returned to the thermal pool. Note that we assume that $\widetilde{C}$ and α remain unchanged (see Fig. 1).

c. Approximation validation

To validate the accuracy of our model, we solve the FP equation numerically for a freely cooling via a Crank-Nicholson scheme with a constant timestep of $\Delta t = 10^{-4}$ Myr and 300 logarithmic momentum points. The thermal electron number density varies linearly from 10^{-4} to $10^{-3}\,\mathrm{cm}^{-3}$ and the magnetic field increase linearly from 1 to $10\,\mu$G. We adopt a time interval of 0.1 Myr to compute the cut-offs, which approximate the timestep in hydro-simulation. From the analysis to determine the cut-offs, unlike the finite difference method, which is known to be stable for a certain timestep, our scheme of treating CRE is insensitive to the adopted timestep and suitable for the usage in hydro-simulation. We show the numerically exact solution (solid lines) and approximate (dashed lines) distribution with an initial population described by $(C, \alpha, p_{\mathrm{min}}, p_{\mathrm{max}}) = (1, 2.5, 10^{-2}, 10^{8})$ in Fig.1, from which we find that the approximate treatment captures the evolution of the exact solution reasonably well, the errors of energy and pressure are $\lesssim 4\%$ within 300Myr. The discrepancy at low energy is acceptable for the present purpose since those electrons hardly contribute to the radio emission and the hydro-simulation only cares about the energy and pressure of CRE. Because the low energy part of the electron population is ignored, it is not surprising that the total CRE

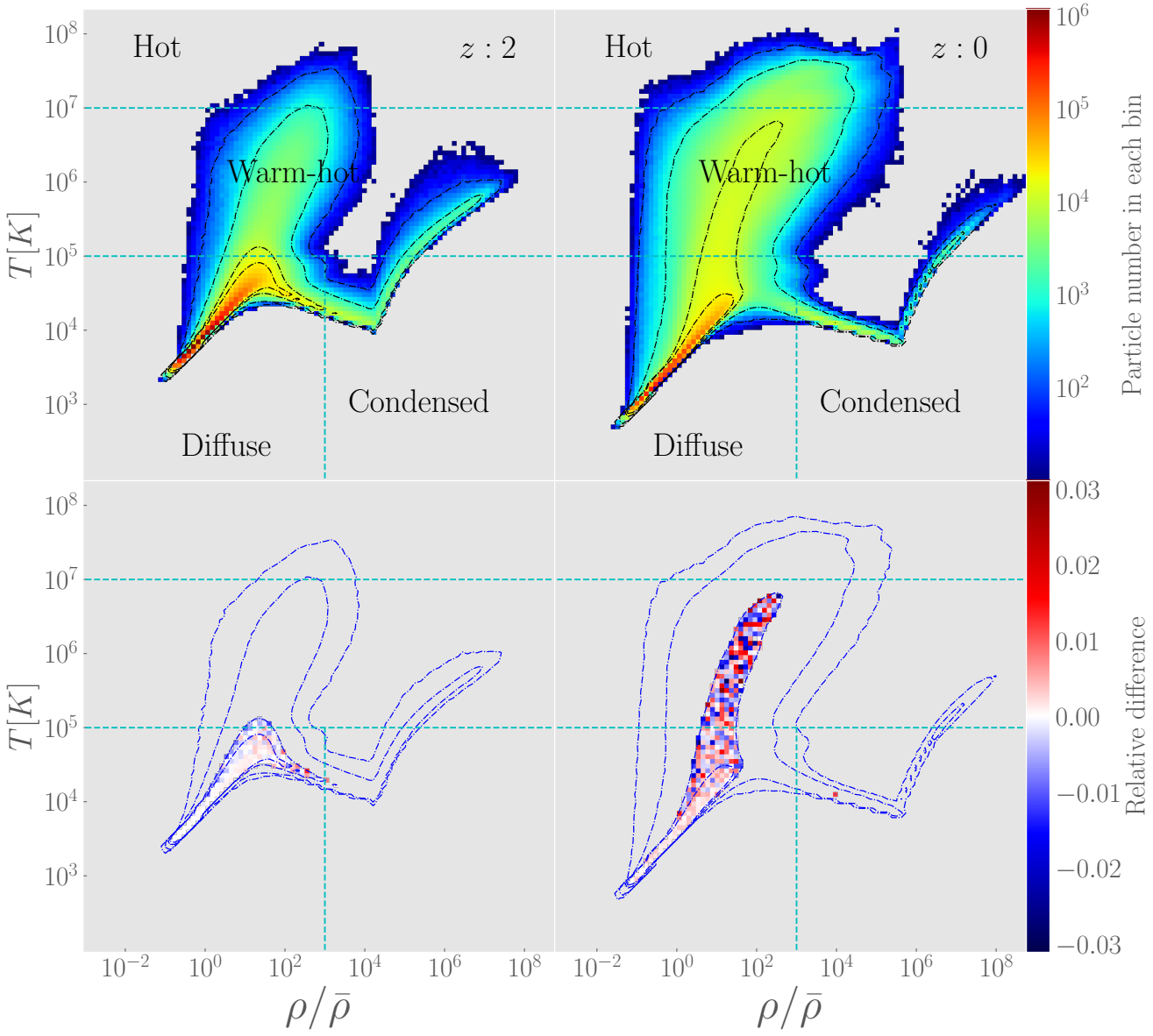


Figure 7. Top: Gas density-temperature phase diagram of SIM simulation at $z = 2$ (left) and $z = 0$ (right). $\bar{\rho}$ is the mean baryonic density, and Contour leves (dashdot line) are placed at 10^2, 10^3, 10^4 and 2×10^4. Bottom: Relative difference of gas phase diagram between SIM and SIM-CRE. In order to avoid the statistical error, we only plot the relative difference for the bins with the particle number larger than 10^4, *Diffuse*: $\rho/\bar{\rho} < 1000, T < 10^5$K. Photoionized intergalactic gas. *Condensed*: $\rho/\bar{\rho} > 1000, T < 10^5$K. Stars and cool galactic gas. *Warm-hot*: 10^5K $< T < 10^7$K. Warm-hot intergalactic medium. *Hot*: $T > 10^7$K. Gas in galaxy clusters and large groups (Davé et al. 2001).

number density is underestimated. For some applications, the accuracy level of our approximation method should be sufficient (Enßlin et al. 2007), even though the energy difference seems to increase after a larger timescale. A more sophisticated treatment of CRE physics may be needed for some application with a requirement of high accuracy level, which is beyond the scope of present work.

2.3.3 *Adiabatic energy changes*

If the electrons are confined within a varying volume, they are subject to adiabatic gains and losses, which are described by

$$\frac{df(p,t)}{dt} = -(\nabla \cdot v) f(p,t). \tag{23}$$

This processes has no effect on the cut-offs and spectral slope and leads to

$$\frac{\widetilde{C}_{t+\Delta t}}{\widetilde{C}_t} = \frac{\tilde{n}_{t+\Delta t}}{\tilde{n}_t} = \frac{\tilde{\epsilon}_{t+\Delta t}}{\tilde{\epsilon}_t} = e^{-\nabla\cdot v\Delta t}. \tag{24}$$

3 SIMULATION

3.1 Simulation setup

For our simulations, we adopt the same cosmological parameters as Marinacci et al. (2015): $\Omega_{\rm m} = \Omega_{\rm dm} + \Omega_{\rm b} = 0.302$, $\Omega_{\rm b} = 0.04751$, $\Omega_\Lambda = 0.698$, $\sigma_8 = 0.817$, $n = 1$ and $H_0 = 68\,{\rm km\,s^{-1}\,Mpc^{-1}}$.

Pfrommer et al. (2006) have pointed out that their scheme of detecting shock has good convergence and used a simulation employed 2×256^3 particles in a periodic box of comoving size $100\,h^{-1}$ Mpc to study the cosmological shock waves. Jubelgas et al. (2008) have used this scheme and picked a comoving box of side-length $100\,h^{-1}$Mpc to simulate their CRP model at two resolutions, with 2×128^3 and 2×256^3 particles, respectively. As they pointed out that the results of their two resolutions are in good agreement with each other. Since the injection source of their CRP model is also the DSA and we use the same method to detect shock waves as them, we chose the resolution with a comoving box of side-length $100\,h^{-1}$Mpc and 2×256^3 particles.

We run two cosmological MHD simulations, named as SIM (without CRE physics) and SIM-CRE (with CRE physics, Fig. B1 of appendix B gives some visualization). Initial condition with $z = 127$ is created by the code 2LPTIC (Crocce et al. 2006) with an Efstathiou power spectrum (Efstathiou et al. 1992), which is based on second-order Lagrangian Perturbation Theory (2LPT), rather than first-order (Zel'dovich approximation). In order to compute the radio background from intergalactic shocks (see Sec. 3.2), we output 142 snapshots within the range of redshift $15 - 0$.

We run Gadget-3 with the default setting of the numerical SPH parameters, using 32 neighbours in smoothed estimates and an artificial viscosity parameter of $\alpha = 0.8$, combined with Balsara's switch (Balsara 1995) to reduce the viscosity in the presence of strong shear. The baryon physics included in our simulation are star formation, cooling processes, shock wave, CRP, and MHD, the settings of which are: **(1) Star formation**, we adopt the model parameters suggested by Springel & Hernquist (2003) and take the number of stars each gas particle may form as 1 (see Springel & Hernquist 2003). **(2) Cooling**, we use the default cooling scheme, the cooling rates of which are given by Katz et al. (1996). **(3) Shock waves**, we use a composite of CRP and thermal gas to derive Mach number and take shock length scale parameter f_h as 2 (Pfrommer et al. 2006). **(4) CRP**, we take the parameters advised by Jubelgas et al. (2008) for the CRP spectrum, the injectons of DSA and supernovae. **(5) MHD**, we use the MHD implementation of Dolag & Stasyszyn (2009) with the hyperbolic/parabolic divergence cleaning scheme originally proposed by Dedner et al. (2002), which has found popular use in in both Eulerian (Mignone & Tzeferacos 2010) and Lagrangian codes (Pakmor et al. 2011), to ensure the $\nabla \cdot B = 0$ constraint, and a limiter proposed by Stasyszyn et al. (2013) to avoid overcorrections due to the cleaning scheme. The hyperbolic, parabolic and limiter paramter are set to 4, 2 and 0.5, respectively (Stasyszyn et al. 2013). In the case of adiabatic the magnetic field evolves as $B = B_0(1+z)^2 \propto \rho^{2/3}$, where B_0 is the rescaled intensity of the B at $z = 0$ or the comoving magnetic field, ρ is the gas density, the structure formation will amplify 10^{-14} comoving Gauss seed fields to the value observed in low-reshift galaxies (Marinacci et al. 2015, 2018), so we use 10^{-10} G as our initial physical magnetic field at $z = 127$.

3.2 Radio emission and observation

In order to verify the rationality of our model, we discuss the computation of radio emission and several results given by our SIM-CRE simulation.

The synchrotron power of a single electron with momentum p in a magnetic field B is (see Rybicki & Lightman 1979; Hoeft & Brüggen 2007)

$$\frac{dP(p,\nu)}{d\nu} = \frac{\sqrt{3}\,B\,e^3\,\sin\,\alpha}{m_e c^2} F\left(\frac{\nu}{\nu_c}\right), \tag{25a}$$

$$F(x) = x\int_x^\infty K_{5/3}(\xi)d\xi, \tag{25b}$$

$$\nu_c = \frac{3\,(1+p^2)\,e\,B\,\sin\,\alpha}{4\pi m_e c}, \tag{25c}$$

where α is the pitch angle, $K_{5/3}$ is the modified Bessel function, and ν_c is the characteristic frequency. The synchrotron emissivity per volume is given by

$$\frac{d^2P(\nu)}{dVd\nu} = \int_0^\infty f(p)\frac{dP(p,\nu)}{d\nu}dp. \tag{26}$$

In SPH, we estimate the synchrotron power of an individual SPH particle at frequency ν by

$$P_{\rm sph}(\nu) = \frac{4}{3}\pi h^3 \frac{d^2P(\nu)}{dVd\nu}, \tag{27}$$

where h is the smoothing length of an SPH particle.

In Fig. 3, we plot baryon density, magnetic field, Mach number, CRE energy, 1.4GHz radio emission and the spectral index in 350MHz − 1.4GHz (from left to right) of most massive cluster at $z = 0.1$ in the SIM-CRE simulation. The magnetic field follows the baryon density distribution, which reaches the largest value at the baryon density peak and decreases quickly with baryon density. There are also some local increases of magnetic field outside the center of the cluster, which corresponds to infalling sub-structures (Marinacci et al. 2015). The CRE energy is very related to the shocks, this is because the only injection source of CRE is shock in our model. The ratio of CRE energy to baryon energy is $\lesssim 0.1\%$, which is consistent with the DSA injection efficiency $\zeta_{\rm DSA} = 0.005$. Due to a weak magnetic field, the radio emission of most CRE is very weak. In Fig. 4, we demonstrate the relation between radio power of 1.4 GHz and the virialization of cluster, where E_k/E_p is the virial ratio which is a direct measure of the dynamical state of a cluster, the radio power tends to increase with increasing $|E_k/E_p + 0.5|$, that is relaxed clusters show much lower radio emission (Buote 2001). The spectral index is a powerful tool to understand the physical properties of radio objects. The spectral data of halo and relic are reported in Table 2 and Table 4 of Feretti et al. (2012), respectively. From Table 2, Table 4 and Figure 18 of Feretti et al. (2012) we know that radio objects have a spectral index within a range $\sim 0.8 - 3$. From last column of Fig. 3, we know that the spectral indices produced by our simulation are consistent with that.

In Fig. 2, we give the integrated CRE distribution and the radio emission of ten most massive clusters. The CRE spectrum is also a power law at high energy. Since the low energy part of the CRE spectrum is ignored in our model and the integrated CRE spectrum

of a cluster is obtained by a summation, it is not surprising that the flattening effect of Coulomb scattering in low energy (Fig. 1) can not be well described by our model, however, this discrepancy does not affect the simulation and the computation of radio emission (see Sec.2.3.2). The spectral index of the integrated radio emission with frequency 100MHz to a few GHz has been estimated to be in the range $0.7-0.8$ (see Section 3.2.2 of Keshet et al. 2004). From Fig. 2, most of the spectral index of integrated radio emission produced by our SIM-CRE simulation are in this range.

Finally, we estimate the radio background emission from our SIM-CRE simulation. The radio background from all particles in the simulation snapshot at redshift z is

$$I(\nu_{\rm obs}, z) = \frac{1}{4\pi D_{\rm lum}^2(z)\Omega} \sum_{i=0}^{N_{\rm gas}} P_{\rm sph,i}[(1+z)\nu_{\rm obs}] \tag{28}$$

where $D_{\rm lum}$ is the luminosity distance and Ω is the solid angle of the simulation box. To obtain the total radio background, one has to integrate Eq. 28 from the low redshift z_1 to the high reshift z_2, that is

$$\begin{aligned} I_{\rm tot}(\nu_{\rm obs}) &= \int_{z_1}^{z_2} dI\,(\nu_{\rm obs}, z) = \int_{z_1}^{z_2} \frac{dI\,(\nu_{\rm obs}, z)}{dD_{\rm com}(z)} \frac{dD_{\rm com}(z)}{dz} dz \\ &\approx \int_{z_1}^{z_2} \frac{I\,(\nu_{\rm obs}, z)}{L} \frac{dD_{\rm com}(z)}{dz} dz \end{aligned} \tag{29}$$

where $D_{\rm com}$ is comoving distance. In this work, we adopt $z_1 = 0.1$ and $z_2 = 5$. Based on the dimensional-analysis model of Waxman & Loeb (2000), Keshet et al. (2004) have estimated the extragalatic radio emission from the strong shocks involved in structure formation. They have predicted that the radio in the frequency range $10-100$MHz is in a range $10^8 - 10^7$mJy sr^{-1} with a spectral index ~ 1 (see Figure.6 of Keshet et al. 2004). We show the radio background emission estimated from Eq. 29 in Fig. 5, from which we learn that the spectral index of our result is 0.74 and the intensity in $10-100$MHz also ranges $10^8 - 10^7$mJy sr^{-1}. Note that the intensity of radio background emission is related to the DSA injection efficiency $\zeta_{\rm DSA}$, so it can be regulated by $\zeta_{\rm DSA}$.

3.3 The impacts of CRE

In this subsection, we investigate the impacts of the CRE processes on the cosmological hydro-simulation.

In Fig. 6, we give Probability Density Function (PDF) of CRE pressure and CRP pressure taken from the snapshot of SIM-CRE simulation with $z = 0$. For most of the gas particles, the ratio of the CRP pressure to the total gas pressure $P_{\rm CRP}/P_{\rm tot}$ ($P_{\rm tot} = P_{\rm bar} + P_{\rm CRP} + P_{\rm CRE}$) is about $0.1-1$, which indicates that the CRP pressure is important to the hydro-simulation (Jubelgas et al. 2008). Since most gas particles with $P_{\rm CRE}/P_{\rm tot} \lesssim 10^{-4}$, the CRE pressure can be ignored in hydro-simulation.

In Fig. 7, we present the $\rho - T$ phase-space diagram (particle number in each bin) of SIM simulation at $z = 2$ and $z = 0$, the relative difference (hereafter "difference") of phase-space diagram between SIM and SIM-CRE are plotted at the bottom. In order to avoid the statistical error, we only plot the difference for the bins with the number of particles larger than 10^4. As shown in the upper panel of Fig. 7, several well-known features can be readily identified (Davé et al. 2001; Vogelsberger et al. 2012):

Diffuse: $\rho/\bar{\rho} < 1000, T < 10^5$K. Photoionized intergalactic gas.

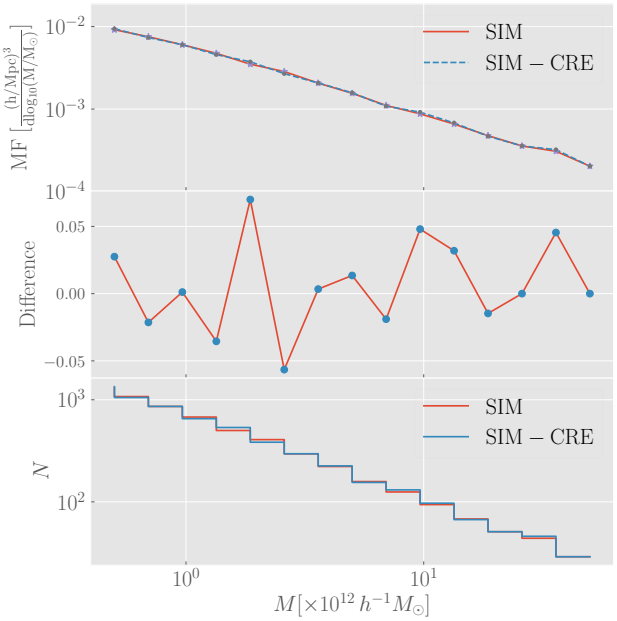


Figure 8. Top: Mass function (MF) at z=0. Middle: Relative difference of MF between SIM and SIM-CRE. Bottom: the number of group in each bin.

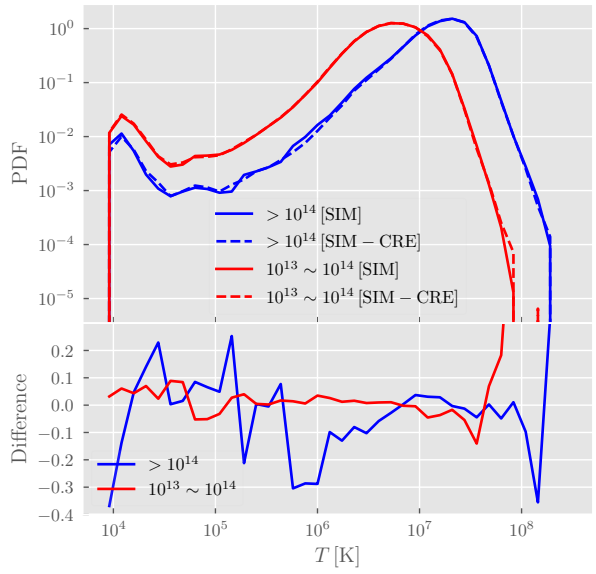


Figure 9. PDF of the gas temperature in the FoF group at $z = 0$. The blue lines in the top panel is the PDF of the gas temperature of all gas particles in the FoF groups with $M > 10^{14}h^{-1}M_\odot$, while the red lines is the slimilar PDF for the FoF groups with $10^{13}h^{-1}M_\odot < M < 10^{14}h^{-1}M_\odot$, The relative difference are shown in the bottom panel. For the FoF groups with $M > 10^{14}h^{-1}M_\odot$, there are about 1500 gas partile in the nearest bin on the right of 10^6K. For the FoF groups with $10^{13}h^{-1}M_\odot < M < 10^{14}h^{-1}M_\odot$, there are about 4000 gas particles in the nearest bin on the right of 10^4K. The unit of mass is $h^{-1}M_\odot$.

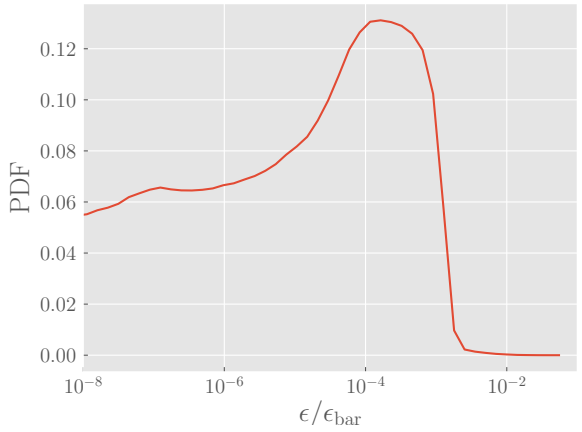


Figure 10. PDF of the CRE energy of particles taken from the snapshot with reshift $z = 0$

Condensed: $\rho/\bar{\rho} > 1000, T < 10^5$K. Stars and cool galactic gas.

Warm-hot: $10^5\text{K} < T < 10^7\text{K}$. Warm-hot intergalactic medium.

Hot: $T > 10^7$K. Gas in galaxy clusters and large groups.

Since the gas with $\rho/\bar{\rho} \sim 10 - 10^4$ and $T \sim 10^5 - 10^7$K is comprised of the shock-heated gas (Vogelsberger et al. 2012) and our injection source of CRE is only DSA, the difference of phase-space state may occur in *warm-hot* phase, from right of Fig. 7, we lean that the influence of the CRE processes on the *warm-hot* intergalactic medium is up to ±3%. The CRE processes does not affect the narrow ridge with $\rho/\bar{\rho} < 10$ and $T < 10^5$K in the diffuse photoionized intergalactic gas, the physics of which are only adiabatic expansion cooling and photoionization heating (Vogelsberger et al. 2012).

In Fig. 8, we plot the mass function of SIM and SIM-CRE at z=0, the difference of mass function between SIM and SIM-CRE (middle panel), and the number of group in each bin (bottom panel), where we apply the FOF algorithm with a link length parameter 0.16 to all particles (Dark Matter, Gas and Star). From the top panel of Fig. 8, we find that the influence of the CRE processes on mass function is up to 5%. Since there are few number of group with $M > 10^{13}\,h^{-1}M_\odot$, the difference of mass function above $10^{13}\,h^{-1}M_\odot$ contain much statistical error.

Finally, we investigate the impacts of the CRE processes on the gas temperature in FoF groups. We plot the PDF of the gas temperature in FoF groups and its the difference between our two simulations in Fig. 9, from which we find that the CRE processes have a slight impact on the gas temperature. To give a relatively reliable result, we neglect bins with an insufficient amount of gas particles (<10^3). For the FoF groups with $M > 10^{14}\,h^{-1}M_\odot$, the largest difference occurs on the right of 10^6K with a difference of $\sim 10\%$ caused by the CRE processes. Similarly, for the FoF groups with $10^{13}\,h^{-1}M_\odot < M < 10^{14}\,h^{-1}M_\odot$, the influence of the CRE processes on the gas temperature will reach about 5%.

To summarize, since the DSA injection efficiency $\zeta_{\rm DSA} = 0.005$, the energy of CRE for most particles are very small compared to the baryon energy (the ratio $\lesssim 0.1\%$, see the fourth column of Fig. 3 or Fig. 10), the accuracy of energy and pressure of our method is > 96% within 300 Myr (see Fig. 1), which guarantees that the result does not deviate too much. However, the CRE processes can cause several percentage points of influence on hydro-simulation, especially on the gas temperature of massive galaxy cluster with $M > 10^{14}\,h^{-1}M_\odot$.

4 SUMMARY

In this paper, we have presented an approximative framework to trace CRE physics and its implementation in hydro-simulation which is capable of carrying out high-resolution simulations of cosmological structure formation with CRE physics.

In our method, we use a simplified power law for the momentum distribution with spatially varying amplitude, upper cut-off, lower cut-off, and spectral index to approximate the real CRE spectrum for each fluid element. The on-the-fly shock detection scheme for SPH developed by Pfrommer et al. (2006) allows us to estimate Mach number, such that we can use DSA with an appropriate efficiency for CRE injection, and then we use the principles of conservation of energy to derive the spectral parameters after DSA injection. Coulomb cooling and radiative cooling mainly occur in low energy and high energy, respectively, in order to account for these cooling and follow the evolution of CRE spectrum after injection, we develop an approximating method to integrate these losses, which reach a balance between the complexity of CRE physics and the requirement of computational efficiency and enable us to determine the cut-offs of CRE spectrum. We also discuss the accuracy of our method by comparing with the numerical solution of FP equation, the dynamical quantities like CRE energy and pressure are reasonably well represented by our method with an accuracy > 96% within 300Myr even if the number density and the distribution at low energy does not match which are unimportant for the use in hydro-simulation and computation of radio emission. We also take the adiabatic gains and losses into account.

Dolag & Stasyszyn (2009) have implemented MHD treatment in SPH-simulation, which allows us to trace the magnetic field in an MHD-simulation and then compute radio emission from the CRE spectrum. The radio flux densities and spectral index for the massive clusters in the simulation are in agreement with observations (Feretti et al. 2012; Keshet et al. 2004), and the radio background of intergalactic shocks estimated from our simulation is consistent with the previous result (Keshet et al. 2004). Our result also shows that relaxed clusters have lower fluxes.

We have present the discussion about the impacts of the CRE processes on the cosmological hydro-simulation. We found that the CRE pressure can be ignored in hydro-simulation, the phase-space diagram of gas is altered up to 3% in *warm-hot* phase, and the influence of the CRE processes on the mass function in the mass range $10^{12} - 10^{13}h^{-1}M_\odot$ is up to 5%. Finally, we discuss the impact of the CRE processes on the gas temperature of the FoF group at $z = 0$, and find that the influence of the CRE processes on the gas temperature of the FoF group with $M > 10^{14}h^{-1}M_\odot$ will reach $\sim 10\%$.

ACKNOWLEDGEMENTS

We are grateful to Volker Springel for his kind offer of the developer version of the Gadget-3 code. All simulations and analysis were performed on the high-performance cluster at Center for Astronomy and Astrophysics (CAA) at Shanghai Jiao Tong University.

This work is supported by the Ministry of Science and Technology of China (grant No. 2018YFA0404601), the National Natural Science Foundation of China (grant Nos. 11433002, 11621303, 61371147), the National Key Research and Discovery Plan (grant No. 2017YFF0210903), and IBS under the project code, IBS-R018-D1.

REFERENCES

Balsara D. S., 1995, Journal of Computational Physics, 121, 357
Brunetti G., Lazarian A., 2011, MNRAS, 410, 127
Brunetti G., Blasi P., Cassano R., Gabici S., 2004, MNRAS, 350, 1174
Bryan G. L., et al., 2014, ApJS, 211, 19
Buote D. A., 2001, ApJ, 553, L15
Cassano R., Brunetti G., 2005, MNRAS, 357, 1313
Chang J. S., Cooper G., 1970, Journal of Computational Physics, 6, 1
Crocce M., Pueblas S., Scoccimarro R., 2006, MNRAS, 373, 369
Davé R., et al., 2001, ApJ, 552, 473
Dedner A., Kemm F., Kröner D., Munz C.-D., Schnitzer T., Wesenberg M., 2002, Journal of Computational Physics, 175, 645
Dolag K., Stasyszyn F., 2009, MNRAS, 398, 1678
Donnert J., Brunetti G., 2014, MNRAS, 443, 3564
Efstathiou G., Bond J. R., White S. D. M., 1992, MNRAS, 258, 1P
Enßlin T. A., Pfrommer C., Springel V., Jubelgas M., 2007, A&A, 473, 41
Feretti L., Giovannini G., Govoni F., Murgia M., 2012, A&ARv, 20, 54
Fermi E., 1949, Physical Review, 75, 1169
Hoeft M., Brüggen M., 2007, MNRAS, 375, 77
Hoeft M., Brüggen M., Yepes G., Gottlöber S., Schwope A., 2008, MNRAS, 391, 1511
Jubelgas M., Springel V., Dolag K., 2004, MNRAS, 351, 423
Jubelgas M., Springel V., Enßlin T., Pfrommer C., 2008, A&A, 481, 33
Katz N., Weinberg D. H., Hernquist L., 1996, ApJS, 105, 19
Keshet U., Waxman E., Loeb A., 2004, ApJ, 617, 281
Landau L. D., Lifshitz E. M., 1959, Fluid mechanics
Lawson K. D., Mayer C. J., Osborne J. L., Parkinson M. L., 1987, MNRAS, 225, 307
Longair M. S., 2011, High Energy Astrophysics
Marinacci F., Vogelsberger M., Mocz P., Pakmor R., 2015, MNRAS, 453, 3999
Marinacci F., et al., 2018, MNRAS, 480, 5113
Mignone A., Tzeferacos P., 2010, Journal of Computational Physics, 229, 2117
Monaghan J. J., 1992, ARA&A, 30, 543
Monaghan J. J., 2005, Reports on Progress in Physics, 68, 1703
Pakmor R., Bauer A., Springel V., 2011, MNRAS, 418, 1392
Park B. T., Petrosian V., 1995, ApJ, 446, 699
Park B. T., Petrosian V., 1996, ApJS, 103, 255
Petkova M., Springel V., 2009, MNRAS, 396, 1383
Pfrommer C., Springel V., Enßlin T. A., Jubelgas M., 2006, MNRAS, 367, 113
Pinzke A., Oh S. P., Pfrommer C., 2017, MNRAS, 465, 4800
Rybicki G. B., Lightman A. P., 1979, Radiative processes in astrophysics
Scholz T. T., Walters H. R. J., 1991, ApJ, 380, 302
Sijacki D., Springel V., Di Matteo T., Hernquist L., 2007, MNRAS, 380, 877
Springel V., 2005, MNRAS, 364, 1105
Springel V., 2010, MNRAS, 401, 791
Springel V., 2011a, arXiv e-prints,
Springel V., 2011b, arXiv e-prints,
Springel V., Hernquist L., 2003, MNRAS, 339, 289
Springel V., Yoshida N., White S. D. M., 2001, New Astron., 6, 79
Springel V., Di Matteo T., Hernquist L., 2005a, MNRAS, 361, 776
Springel V., et al., 2005b, Nature, 435, 629
Stasyszyn F. A., Dolag K., Beck A. M., 2013, MNRAS, 428, 13
Vazza F., Dolag K., Ryu D., Brunetti G., Gheller C., Kang H., Pfrommer C., 2011, MNRAS, 418, 960
Vogelsberger M., Sijacki D., Kereš D., Springel V., Hernquist L., 2012, MNRAS, 425, 3024
Vogelsberger M., et al., 2014, Nature, 509, 177
Waxman E., Loeb A., 2000, ApJ, 545, L11

APPENDIX A: FORMULA

The incomplete Beta function is

$$B_x(a,b) = \int_0^x t^{a-1}(1-t)^{b-1}\,dt. \tag{A1}$$

We introduce the symbol B_{mn}, i.e.

$$B_{mn} = \frac{1}{2}B_{\frac{1}{1+q^2}}\left(\frac{\alpha-m}{2}, \frac{n-\alpha}{2}\right). \tag{A2}$$

The relations between the dimensionless velocity, the Lorentz factor and the dimensionless momemtum are

$$\beta = \frac{p}{\sqrt{1+p^2}}, \quad \gamma_L = \sqrt{1+p^2}. \tag{A3}$$

So

$$\frac{d\gamma}{dp} = \beta, \quad \frac{d\beta}{dp} = \frac{1}{\gamma^3}. \tag{A4}$$

Defining $t = \frac{1}{1+p^2}$, we get

$$\begin{aligned} p &= \left(\frac{1-t}{t}\right)^{\frac{1}{2}} \\ \frac{dp}{dt} &= -\frac{1}{2}\frac{t^{-\frac{3}{2}}}{\sqrt{1-t}}, \end{aligned} \tag{A5}$$

from which we can do the following useful integrals,

$$\begin{aligned} &\int_q^\infty \frac{p^{-\alpha}}{\sqrt{1+p^2}} = \int_{\frac{1}{1+q^2}}^0 \left(\frac{1-t}{t}\right)^{\frac{-\alpha}{2}} t^{\frac{1}{2}}\left(-\frac{1}{2}\frac{t^{-\frac{3}{2}}}{\sqrt{1-t}}\right)dt \\ &= \frac{1}{2}\int_0^{\frac{1}{1+q^2}} t^{\frac{\alpha}{2}+\frac{1}{2}-\frac{3}{2}}(1-t)^{\frac{-\alpha}{2}-\frac{1}{2}}\,dt \\ &= \frac{1}{2}\int_0^{\frac{1}{1+q^2}} t^{\frac{\alpha}{2}-1}(1-t)^{\frac{1-\alpha}{2}-1}\,dt \\ &= \frac{1}{2}B_{01}, \end{aligned} \tag{A6}$$

and

$$\begin{aligned} &\int_q^\infty \sqrt{1+p^2}p^{-\alpha}dp = \int_q^\infty \sqrt{1+p^2}\frac{dp^{1-\alpha}}{1-\alpha} \\ &= \frac{1}{\alpha-1}q^{1-\alpha}\sqrt{1+q^2} \\ &- \int_q^\infty \frac{p^{2-\alpha}}{(1-\alpha)\sqrt{1+p^2}} \\ &= \frac{1}{\alpha-1}\left[\frac{1}{2}B_{23} + q^{1-\alpha}\sqrt{1+q^2}\right]. \end{aligned} \tag{A7}$$

So the CRE energy ϵ and pressure P are given by

$$\begin{aligned} \epsilon &= \int_q^\infty mc^2\left(\sqrt{1+p^2}-1\right) \quad Cp^{-\alpha}dp \\ &= \frac{Cmc^2}{\alpha-1}\left[\frac{1}{2}B_{23} + q^{1-\alpha}\left(\sqrt{1+q^2}-1\right)\right], \end{aligned} \tag{A8}$$

$$
\begin{aligned}
P &= \int_q^\infty \frac{m_e c^2 \beta p}{3} \quad C p^{-\alpha} dp \\
&= \frac{Cmc^2}{3} \int_q^\infty \frac{p^{2-\alpha}}{\sqrt{1+p^2}} dp \\
&= \frac{Cmc^2}{6} B_{23}.
\end{aligned}
\tag{A9}
$$

APPENDIX B: VISUALIZATION

This paper has been typeset from a TEX/LATEX file prepared by the author.

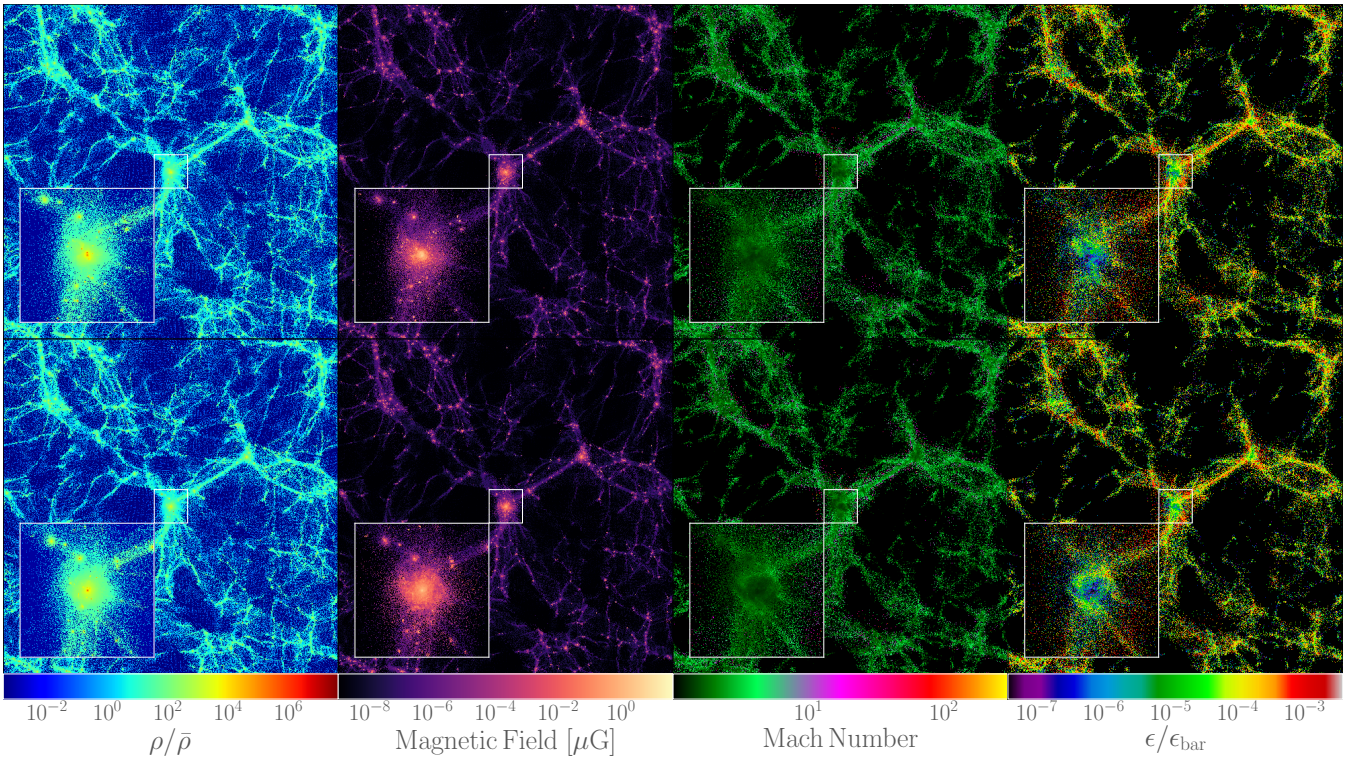


Figure B1. Visulization of SIM-CRE at redshift $z = 0.1$ (top panels) and $z = 0$ (bottom panels). These pictures have a comoving side length of $100\,\mathrm{h}^{-1}$Mpc while the projection length along the line of sight amounts to $10\,h^{-1}$Mpc. The zoom-in plot extents $10\,h^{-1}$Mpc and contains the most massive cluster in slimulation.